

Noninvasive beam-size measurements for linear induction acceleratorsC. Ekdahl^{1,*}, H. V. Smith¹, W. B. Broste², H. A. Bender¹, N. D. Kallas¹, K. McCurdy¹,
D. C. Moir¹, M. Sanchez¹, G. P. Salazar¹ and W. C. Ogg¹¹Los Alamos National Laboratory, P.O. Box 1663, Los Alamos, New Mexico 87545, USA²Keystone International, 8224 Louisiana Blvd Suite D, Albuquerque, New Mexico 87113, USA

(Received 27 June 2022; accepted 20 September 2022; published 6 October 2022; corrected 11 April 2023)

Diamagnetic loops (DML) can be used as a noninvasive method for the measurement of beam size in electron beam accelerators that use solenoidal magnetic transport. The loop fundamentally measures the magnetic flux excluded by a diamagnetic object. A comprehensive theory relates the rms beam radius to the excluded flux measured by the DML. We have built and calibrated a DML apparatus. Recently, this DML has been used to measure the size of the electron beam near the final focus of a flash-radiography linear induction accelerator. The results are in agreement with predictions from transport code simulations. In this article, we review and summarize the construction, calibration, and electron-beam testing of this DML.

DOI: [10.1103/PhysRevAccelBeams.25.102801](https://doi.org/10.1103/PhysRevAccelBeams.25.102801)**I. INTRODUCTION**

Flash radiography of explosively driven hydrodynamic experiments is a diagnostic technique used worldwide [1,2]. This technique employs a modestly intense relativistic electron beam (IREB) to produce a bremsstrahlung-radiation source spot for point projection radiography with a pulse short enough to stop the hydrodynamic motion of the object.

As practiced at the Los Alamos dual-axis radiographic hydrodynamic testing (DARHT) facility, the IREBs produced by two linear induction accelerators (LIA) are focused on source spots for radiographs from two different directions. The DARHT-I LIA accelerates a single 60-ns pulse to 19.7 MeV, with peak current ranging from 1.5 to 1.8 kA [3]. The DARHT-II LIA produces up to four 1.7-kA, 16.6-MeV pulses [4–6] with full width at half maximum (FWHM) ranging from 10 to 100 ns and interpulse separation ranging from 100 ns to more than 1000 ns [7,8]. In addition to beam target physics, the minimal spot size is dictated by beam emittance, motion, final-focus solenoid magnet aberrations, and the beam size entering the final-focus magnet. It follows that a real-time monitor of beam size at the entrance to the final-focus magnet would be exceptionally useful for tuning the LIA to achieve the minimal spot size. Moreover, such a diagnostic would

inform efforts to mitigate effects such as envelope oscillations, halo growth, and ion neutralization that cause emittance growth that degrades the focal spot size and radiographic resolution. A diamagnetic loop (DML) can provide this critical information.

The DML diagnostic technique fundamentally measures the magnetic flux excluded by a diamagnetic object in an external magnetic field. The excluded flux measurement is then related to the sought-after physical property of the object through a model; perhaps with the help of additional measurements from other diagnostics. Whether the result is the energy of a plasma column [9,10], the size of a charged particle beam [11], the velocity of a metal projectile or jet, or the susceptibility of a diamagnetic salt, the uncertainty of the result directly depends on the accuracy of the excluded flux measurement. Therefore, a primary calibration must also be directly related to the excluded flux, rather than to a physical property of the diamagnetic object that is inferred through a model and auxiliary measurements. In this way, the fundamental calibration is free of any assumptions and approximations made in relating the properties of the object to the excluded flux.

The size of an IREB can be deduced from DML measurements [11–16]. A rotating IREB generates an internal axial flux opposing the external field (diamagnetism). The measurement of this flux can be related to the beam size with little error for the beam energy relevant to our radiography accelerators. The measurement is time resolved and noninvasive, so it can be used as an online monitor of beam size. For example, for a radiographic LIA, the radiation source spot depends on the beam size entering the final-focus magnet, so a DML at that location would inform tuning for the minimum spot size, which gives a maximum radiographic resolution.

*cekdahl@lanl.gov

Published by the American Physical Society under the terms of the *Creative Commons Attribution 4.0 International* license. Further distribution of this work must maintain attribution to the author(s) and the published article's title, journal citation, and DOI.

Here we describe DML measurements of the IREB produced by the DARHT-I LIA. The measurement is difficult, at best, and can be plagued by external noise sources. Early DML experiments were hampered by spatially limited detection area and the use of transport-solenoid fringe fields [11,12]. Our present work has focused on greatly improving the signal-to-noise ratio (S/N) to reduce the uncertainty in the deduced IREB size. This was achieved by creating a stand-alone apparatus with greatly increased detection area, operating in its own independently controlled bias magnetic field, along with a balanced detector to eliminate the common mode background.

In what follows, we review the theory in Sec. II, describe the DML apparatus in Sec. III, and explain the calibration in Sec. IV. An accounting of the DARHT-I tests is given in Sec. V, with results presented in Sec. VI. We discuss these results and validation of the technique in Sec. VII and offer some concluding remarks in Sec. VIII.

II. THEORY

In its simplest form, the DML technique is illustrated in Fig. 1. A very long conducting beam pipe with radius R_W initially contains a uniform axial magnetic field B_0 . The introduction of an electron beam pulse with radius a depresses the field inside the beam due to beam rotation. The field outside of the beam ($r > a$) is increased by an increment, ΔB , to conserve flux inside of the pipe.

Consider a single loop with radius R_L and area $A_L = \pi R_L^2$ centered within a cylindrical vessel with radius R_W and area $A_W = \pi R_W^2$. For our application, the outer vessel is a conductor that conserves rapid changes of flux. Also, suppose that the vessel is filled with a uniform axial magnetic field B_0 . Now introduce a diamagnetic object as shown in Fig. 1. In our case, the object is a charged particle beam, but it could also be a plasma column, a bullet fired from a gun, or a diamagnetic salt. Inside the object, the field decreases due to diamagnetism. Outside of the object, the field increases to conserve flux.

A. Excluded flux

The flux excluded from the object is defined as [9]

$$\Phi_x \equiv (B_0 + \Delta B)A_a - \int_0^a B_z(r)2\pi r dr, \quad (1)$$

where $A_i = \pi R_i^2$. From flux conservation, one has

$$B_0 A_W = (B_0 + \Delta B)(A_W - A_a) + \int_0^a B_z(r)2\pi r dr, \quad (2)$$

which simplifies to

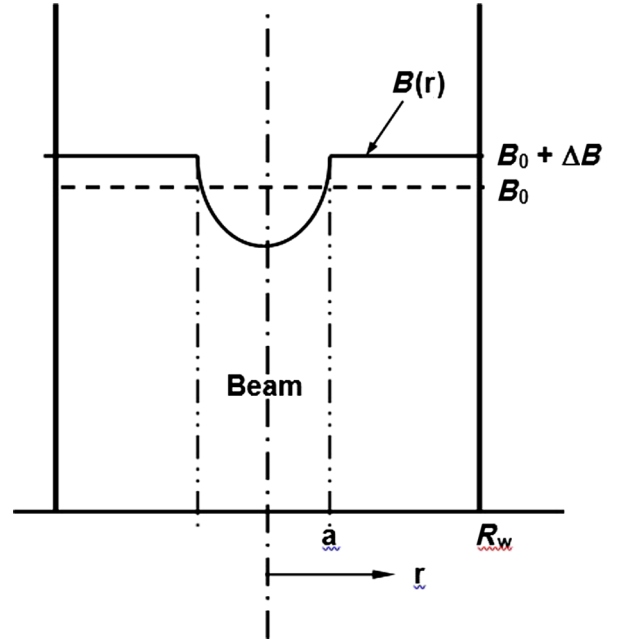


FIG. 1. Magnetic fields inside diamagnetic loop diagnostic. B_0 is the field prior to the arrival of the beam. The field is depressed inside the beam by its diamagnetism. Outside of the beam, the field is increased by ΔB to conserve flux (Adapted from Ref. [14]).

$$\Phi_x = \Delta B A_W. \quad (3)$$

We measure the change in flux through a DML surrounding the object, which is

$$\Delta\Phi_L = (B_0 + \Delta B)(A_L - A_a) + \int_0^a B_z(r)2\pi r dr - B_0 A_L, \quad (4)$$

which simplifies to

$$\Delta\Phi_L = \Delta B A_L - \Phi_x. \quad (5)$$

Using Eq. (3), one has

$$\Delta\Phi_L = -\left(1 - \frac{A_L}{A_W}\right)\Phi_x. \quad (6)$$

This relation clearly shows the advantage of a large annular area between the loop and wall for improving the S/N of $\Delta\Phi_L$ measurements of a given excluded flux. It remains to relate the excluded flux to a model of the object.

B. Rigid-rotor excluded flux

The relation between beam size and excluded flux can be deduced from a rigid-rotor model of beam equilibrium [17–19]. Linear induction accelerators used for radiography employ a reverse field solenoid (“bucking coil”) to null the

magnetic flux linking the cathode, thereby zeroing the canonical angular momentum. This arrangement is often called a shielded cathode. The perfect geometry for this would be a pair of identical coils with equal, but opposite sign, currents, for which the axial field in the midplane containing the cathode is exactly zero, independent of radius.

To conserve canonical angular momentum P_θ , a beam born without any must rotate when it subsequently enters an axial magnetic field. Consider a uniform beam with current I_b and radius a rigidly rotating in an axial magnetic field B_z . The angular frequency of rotation ω can be deduced from conservation of canonical angular momentum:

$$P_\theta = \gamma m_e a^2 \omega - e a^2 B_z / 2 = 0, \quad (7)$$

where γ is the Lorentz relativistic factor. For the DARHT LIAs, the beam is born in a shielded diode, $P_\theta = 0$, so

$$\omega = \frac{e B_z}{2 \gamma m_e}, \quad (8)$$

which is just the betatron frequency. In practical units $\omega = c k_\beta = c(\text{cm/s}) B_z(\text{kG}) / 3.4 \gamma$. Therefore, the azimuthal current density in the beam is

$$j_\theta = n e v_\theta = n e r \omega, \quad (9)$$

where the density is a constant $n e = J_z / \beta c$. Taking the beam to be infinitely long compared to the DML apparatus, one can calculate the increment of the diamagnetic magnetic field dB_D inside a shell of thickness dr to be

$$dB_D = \mu_0 j_\theta dr \quad (10)$$

giving

$$B_D = -\mu_0 \frac{\omega J_z}{\beta c} \int_0^r r dr = -\mu_0 \frac{\omega J_z r^2}{2 \beta c}. \quad (11)$$

Integrating this field over the beam area gives the flux excluded by the rotating beam,

$$\Phi_x = -\mu_0 \frac{\omega J_z}{2 \beta c} \int_0^a r^2 2 \pi r dr. \quad (12)$$

Integrating, one gets

$$\begin{aligned} \Phi_x &= -\mu_0 \frac{\omega J_z \pi a^4}{4 \beta c} \\ &= -\mu_0 \frac{\omega a^2 I_b}{4 \beta c} \\ &= -\mu_0 \frac{e B_z}{2 m_e c \beta \gamma} \frac{I_b a^2}{4} \\ &= -\frac{I_b}{2 I_A} \pi a^2 B_z, \end{aligned} \quad (13)$$

where equilibrium beam rotation at the betatron frequency has been used, and $I_A = \frac{4 \pi m_e c}{\mu_0 e} \beta \gamma = 17.05 \beta \gamma$ kA is the Alfvén limiting current. In much of the IREB literature, the constant multiplier in Eq. (13) is known as the Budker ratio, $\nu / \gamma = I_b / I_A$, where ν is the charge line density normalized to the classical electron radius. For typical radiography LIAs $\nu / \gamma \ll 1$, so high S/N measurements of small beams require the use of large bias fields, much larger than usually available in the fringe fields of focusing solenoids.

Thus, one has the beam rms radius in terms of the measured excluded flux and known B_z , I_b , and γ :

$$\pi R_{\text{rms}}^2 = -\frac{I_A \Phi_x}{I_b B_z}, \quad (14)$$

where $R_{\text{rms}} = a / \sqrt{2}$ and Φ_x is related to the diamagnetic loop measurement by Eq. (6). This is the same as Eq. (48) in Ref. [14], which was derived more rigorously for an arbitrary axisymmetric current distribution. In Ref. [14], it was shown that the error in this approximation for the radius is less than 0.1% for any reasonable current distribution at the beam energy and current of our DARHT-I experiments. In Eq. (6), the factor of proportionality is that of an ideal infinitely long beam pipe of constant radius. Careful calibrations determined the actual factor to be used for our apparatus.

III. APPARATUS

According to Eq. (13), the largest DML signals (highest S/N ratio) will be obtained for large high-current, low-energy beams in a strong magnetic field. The only operational control the experimenter has over this is the bias magnetic field, so our apparatus incorporates a dedicated solenoid to provide the bias field, rather than relying on the fringe field of existing transport solenoids as was the case in earlier experiments. Among other advantages, this permits flexible selection of placement of the DML in drift regions. In use as an installed beam monitor, the DML solenoid can be integrated into the overall magnetic transport tune once it has been adjusted to provide adequate DML signal amplitude.

An advantage of incorporating a dedicated bias solenoid is that it permits enlarging the detection area, which is the area between the loop and the wall, as clear from Eq. (6). Thus, our apparatus has an outer wall diameter of about twice the DML diameter, which was not possible in previous attempts on DARHT-II [20], which suffered from weak S/N.

A. Overview

This diamagnetic loop uses three improvements over previous designs, following the principles of Eqs. (6) and (13). First, the diamagnetic loop is placed in a solenoid

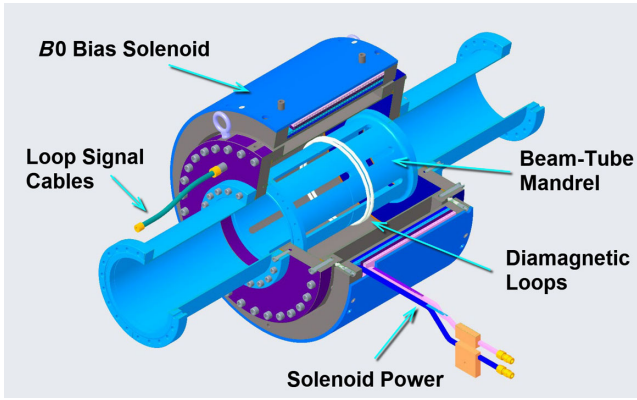


FIG. 2. DML apparatus. The bias solenoid is shown in purple. The beam pipe is shown in blue and the flux-conserving outer wall is shown in gray. Balanced-loop signal output cables are shown in green (Adapted from Ref. [21]).

magnet whose field strength can be independently adjusted to give a desired signal level, as described by Eq. (13), with the detected signal strength being proportional to the external magnetic field. Previous designs have relied on weak, stray magnetic fields from nearby beamline solenoids. Second, the outer flux-conserving conductor is almost twice as large as the diamagnetic loop itself, therefore the Eq. (6) factor $[1 - A_L/A_W] = 0.72$. This is twice the factor of the DARHT-II design ($[1 - A_L/A_W] = 0.36$), where the loop size was constrained to be a larger fraction of the wall size to prevent intercepting large beams with large centroid offsets. Finally, we employ two counter-wound diamagnetic loops to double the signal and eliminate any common mode signals.

The design, fabrication, assembly, and calibration of the DML are detailed in Ref. [21]. Figure 2 is an illustration of our prototype DML apparatus. Nonmagnetic materials (stainless steel and copper) were used throughout the fabricated apparatus. Relevant dimensions are listed in Table I.

TABLE I. DML apparatus dimensions [21].

Element	Symbol	Units	Value
Beam pipe			
Inner radius	R_{in}	cm	7.30
Outer radius	R_{out}	cm	7.94
Slots	N_S		8
Slot length	L_S	cm	25.40
Slot width	w_S	cm	1.27
Sensing can			
Inner radius	R_W	cm	14.92
Length	L_W	cm	30.48
Flux loop			
Radius	R_L	cm	7.916
Wire diameter	d_{wire}	mm	0.1024

B. Balanced flux-detection loops

Time-varying magnetic flux linking the loops generates a voltage signal equal to the electromotive force $\mathcal{EMF} = d\Phi_L/dt$. This DML apparatus uses two opposing single turn loops for balanced signal detection. Since the time derivative of the flux signal on each loop is the opposite sign from the counter-wound loop, differencing the two results in twice the wanted signal and cancels any common mode. For example, let the wanted time derivative of the flux signal be V_Φ and the common mode signal be V_{CM} . Then, the total signal for one of the loops is $V_1 = V_\Phi + V_{CM}$, while for its counterpart $V_2 = -V_\Phi + V_{CM}$, and the difference is $V_1 - V_2 = 2V_\Phi$. Division by two gives a voltage equal to the rate of change of flux, devoid of common mode due to capacitive coupling of the loops to the beam space charge, beam spill onto the wires, radiation-generated cable currents, electrical noise from pulsed power, or similar effects.

The two loops were wound on a mandrel that is a section of the stainless-steel beam tube. The loop wires reside inside a groove machined in the outer wall of the mandrel. The groove is only slightly larger than the insulated No. 18 magnet wire of the loops, which provides accurate alignment of the loop area normal to the beam-line axis.

There are eight longitudinal slots machined in the mandrel to allow the loops to respond to the fast diamagnetic perturbation in the axial magnetic field caused by the electron beam. The wide sections of the tube between slots

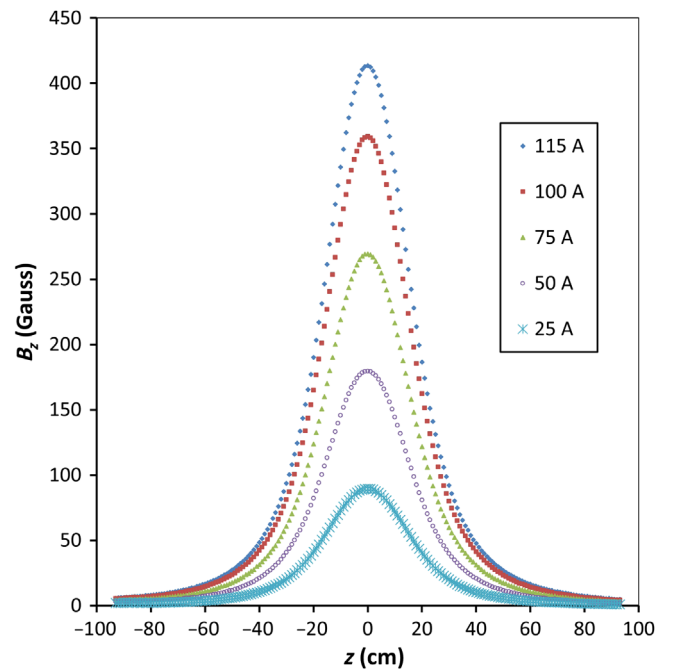


FIG. 3. Magnetic bias field on axis of the DML apparatus for differing values of the solenoid drive current, as indicated in the legend.

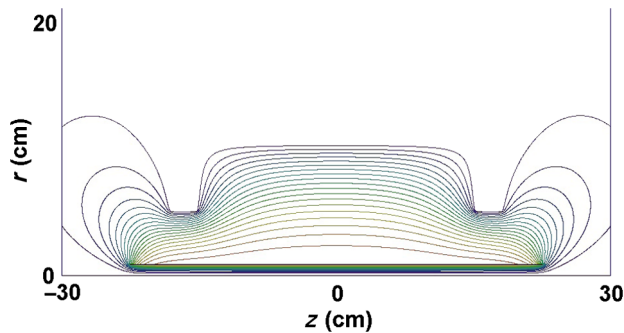


FIG. 4. Magnetic field of calibration coil in the DML apparatus as calibrated.

provide some degree of shielding of capacitive pickup from beam space charge.

C. Bias field solenoid

The diamagnetic loop was immersed in a solenoidal magnetic field of known strength to provide the bias field required by Eq. (14) for the calculation of the rms beam radius from the measured excluded flux and beam current. The loops shown in Fig. 2 were located to be at the maximum field at the center of the solenoid. The solenoid magnet was mapped for different driving currents, and the field on axis is shown in Fig. 3. According to this mapping, it only takes 28 A to generate a 100-G magnetic field, which is sufficient for measurements of the DARHT beam.

This solenoid magnet is also a focusing element in the beam transport line. Fortunately, the strength of the magnetic field only needs to be ~ 100 Gauss to obtain a measurable voltage signal from the diamagnetic loop, and this has little effect on the transport of a 20-MeV beam.

IV. CALIBRATION

In Eq. (6), the factor of proportionality is that of an ideal infinitely long beam pipe of constant radius. Careful calibrations determined the actual factor to be used for our apparatus having finite and three-dimensional (3D) geometry. Our method used long, small-diameter coils driven by a high-voltage, short-pulse generator to provide the excluded flux. The excluded flux was directly measured with a loop tightly wrapped around the calibration coil. The calibration factor was then calculated directly from flux measurements [21]

$$k_{\text{DML}} \equiv \left| \frac{\Delta\Phi_{\text{Loop}}}{\Phi_x} \right|. \quad (15)$$

Due to the nonideal geometry of the real apparatus, this measured factor deviates from the factor for an ideal coaxial geometry of infinite length

$$k_{\text{DML}} = 1 - A_{\text{loop}}/A_{\text{Wall}}. \quad (16)$$

Although calibration is independent of the bias magnetic field, as can be seen by the setting $B_0 = 0$ in deriving Eq. (6), we performed calibrations with and without the bias field. Based on measurements using coils with diameters between 1.59 and 5.08 cm, the average measured calibration factor was $k_{\text{DML}} = 0.655 \pm 1.7\%$ for our prototype [21]. The factor for an infinitely long system calculated from the dimensions in Table I would be $k_{\infty} = 0.72$. The 10% difference is due to the finite apparatus dimensionality, including 3D effects.

We undertook a number of numerical experiments to better understand the factors contributing to the difference between the measured calibration and the ideal in an effort to assess the overall uncertainty that might be expected in beam measurements at DARHT. The PerMag magnetic field solver was used to simulate calibration of the DML [22,23] in a two-dimensional (2D), azimuthally symmetric geometry, but including finite axial dimensionality (see Fig. 4). The indentations of the field at ± 20 cm are due to the end flanges shown in Fig. 2, and absence of externally attached beam tubes, which were removed for calibrations.

The simulated calibration factor using as-built dimensions is $k_{\text{DML}} = 0.70$, which is 2.8% less than the ideal factor (0.72) and differs from the measured value (0.655 [21]) by 7%. To explore finite length effects, different calibration coil lengths were modeled. We also analyzed the effect of adding a beam tube at the ends of the apparatus, but those results showed little effect on the calibration factor. Since this simulation is an accurate 2D model of the calibration experiments, the remaining difference is tentatively ascribed to 3D effects, such as the slotted conducting mandrel.

V. BEAM EXPERIMENTS

The prototype DML apparatus was tested on the single-pulse DARHT-I linear induction accelerator [24].

A. Installation

The DML apparatus was installed in the downstream transport (DST) region from the LIA exit to the radiation target (Fig. 5). The DST region includes two beam-focusing solenoids (DT-1 and DT-2) that precede the

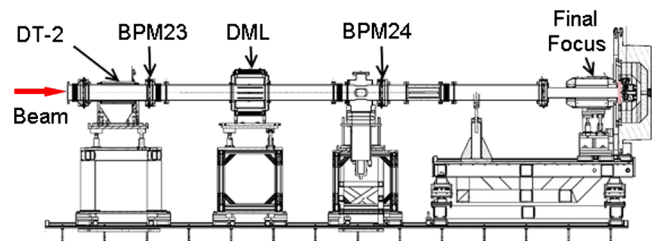


FIG. 5. DML installation in DARHT-I downstream transport.

TABLE II. Location of DST elements.

Element	Name	XTR Name	Position ^a (cm)
LIA exit	Exit	exit#8	3430.300
Solenoid	DT-1	Pherm	3658.700
Solenoid	DT-2	Cellmag	4296.827
Position/current monitor	BPM23	bpm23	4329.242
Solenoid	DML	Dmlp	4429.023
Flux loop	Detector		4429.023
Position/current monitor	BPM24	bpm24	4562.419
Solenoid	Final focus	darhtff	4770.400

^aReferenced to cathode surface at $z = 0$.

DML location, which was near the final-focus (FF) solenoid outside of the accelerator building. The positions of elements of the DST were determined with laser tracker measurements. The location of elements relevant to experimental results is listed in Table II.

B. Electron beam

For these tests, the 64-cell DARHT-I accelerator produced a single 1.51-kA pulse of 19.74-MeV electrons with shot-to-shot reproducibility better than $\pm 0.2\%$ for energy and $\pm 0.4\%$ for current (Table III). The beam pulse could be prevented from exiting the accelerator building by using a radiation-blocking beam stop. This is designated as Mode 1 operation, whereas allowing the beam outside to the final focus is designated as Mode 2.

C. Experiments

Tests with beam were carried out from February 15, 2022, through February 17, 2022. During these DML tests, four different bias field settings were used to validate the linearity of excluded flux with a bias field as determined by Eq. (13). Additional data were taken with no bias field to ascertain nondiamagnetic backgrounds that must be subtracted from the loop flux measurement to obtain the diamagnetic excluded flux. Furthermore, the field of the DT-1 solenoid was varied to produce three different beam radii to validate the quadratic scaling of excluded flux with

TABLE III. Electron-beam parameters.

Parameter	Symbol	Units	Value
Kinetic energy	KE	MeV	19.74
	γ		39.552
	$\beta\gamma$		39.539
Current ^a	I_b	kA	1.51
Pulse width	FWHM	ns	76
Flattop width ^b		ns	64

^aMean value of flattop region.

^b>95% of mean flattop current.

TABLE IV. Number of beam shots vs magnetic field.

	DML bias field, B_0 (G)					
	0	25	50	100	200	
DT-1 (kG)	0.8	3	0	3	5	3
	1.1	1	0	1	1	1
	1.4	1	1	3	3	3

beam size as given by Eq. (13). Thus, validation of the experimental DML method was based on the matrix of magnet settings in Table IV, listing the various combinations for which beam data were acquired and analyzed. The highest S/N ratio was obtained for 50-A DT-1 solenoid current (0.80-kG peak field) and 56-A DML bias solenoid current ($B_0 = 201$ G).

D. Analysis

DML data were recorded with a LeCroy HD08108 12-bit digitizer at 5-Gs/s in the DARHT-I power hall in rack cluster 5. Pretesting with fast pulses injected directly into the 178-ns cables from the DML established the cable attenuation. Beam position monitor (BPM) data were recorded with Keysight M9703B 12-bit digitizers at 2 Gs/s, also in the power hall using cable runs of similar length and attenuation.

Time-resolved results shown in this article are the result of a hand calculation of beam size from data recorded for a shot with DST tuned to produce the largest beam, and with the bias field set for 200-G maximum, thereby giving the largest available S/N. This procedure was coded into a user application written in IDL [25] for further analyses.

DML data were analyzed by correcting for cable response, and then differencing and integrating the two balanced detector loop signals to obtain the measured flux, presumably devoid of common mode. The resulting flux was typically a few tens of nV s. With the DML bias field turned off, there was a persistent background. Since the desired diamagnetic excluded flux is proportional to the bias field for an azimuthally symmetric system with zero flux linking the cathode [14], this background would not be due to beam diamagnetism. Therefore, it was subtracted from the measured flux for the nonzero bias field under the assumption of perfect transport symmetry and cathode shielding.

The BPM and DML data were recorded with digitizers having different time bases. In the absence of accurate cross timing, we established common timing between the current and the excluded-flux pulses by observing that the diamagnetic field is proportional to the current [see Eq. (11)]. Therefore, we aligned the current pulse full-width at half maximum (FWHM) with the excluded-flux FWHM to establish common timing for our analysis. Any uncertainty of the timing of signals leads to large errors during the beam-head rise time and beam-tail fall time, such as either

the calculated displacement or beam size apparently greater than the beam pipe dimensions. Consequently, we have limited our analysis to the flattop region of the current pulse, which varies by no more than 6% no matter the timing assumed. We estimate the resulting uncertainty due to this timing ansatz is less than $\pm 6\%$ for excluded flux and less than $\pm 3\%$ for rms radius.

VI. EXPERIMENTAL RESULTS

We begin our presentation of results with an illustrative example of the analysis of data from a single shot. The diamagnetic data are from shot 37858, for which the DML bias field was 201 G, and the DT-1 solenoid peak field was 0.8 kG, thereby maximizing the signal for best S/N. The zero-bias background shot used for this analysis was shot 37853. The analysis was carried out by hand with the aid of our DAAAC [26] data acquisition, analysis, archival, and control software.

A. Loop flux

Balanced-loop data ($\mathcal{EMF} = d\Phi/dt$) were corrected for cable response, integrated, and differenced to eliminate common mode. Division by 2 yields the loop flux. This is illustrated in Fig. 6 for the mentioned high S/N, large beam size shot 37858. Figure 6 also shows the flux calculated from the low-level background signal of a shot with no DML bias field applied. Since there is no bias field, this background cannot be due to flux excluded from a rotating beam, unless there is flux linking the cathode. We subtract this background under the assumption that the bucking coil perfectly nulls the flux linking the cathode.

B. Excluded flux

The resulting background-corrected flux was divided by the experimentally determined calibration constant to give the desired excluded flux due to diamagnetism, as shown in Fig. 7 for the high S/N ratio shot 37858.

Also shown in Fig. 7 is the flattop of the beam current used for the calculation of beam size. Over this 64-ns flattop, the current was within 95% of the mean $\langle I_b \rangle = 1.51 \text{ kA} \pm 2.3\%$.

C. Time-resolved beam size

To calculate the beam radius for excluded flux, one needs beam distribution-mean momentum ($\beta\gamma$) and current (I_b) for Eq. (14). The result is shown in Fig. 8. For this plot, the momentum was assumed constant $\beta\gamma = 39.539$, and the flattop current used is shown in Fig. 7. The average radius during this flattop is $2.23 \text{ cm} \pm 5.7\%$ standard deviation. The calculated radius is significantly larger outside of the flattop due to the rapidly varying current. Moreover, there are significant errors during the beam head and tail due to the lack of accurate timing correlation between DML and BPM data.

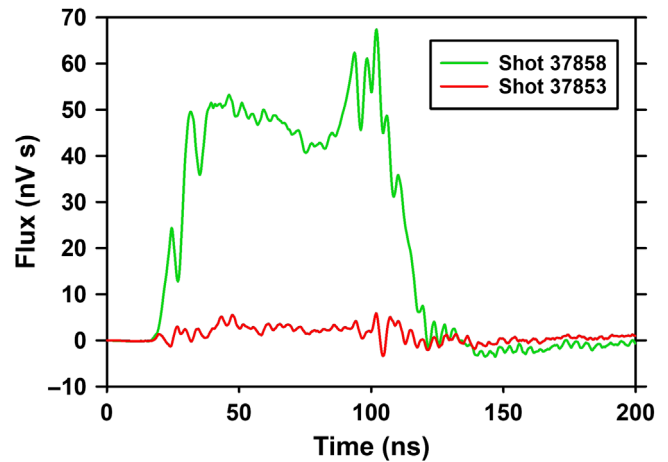


FIG. 6. Integrated loop-flux signal from a shot with 200-G bias field (green curve) compared with the integrated loop-flux signal from a background shot with zero bias field (red curve). (The baseline errors long after the pulse are due to the first-order approximation to correction for cable distortion).

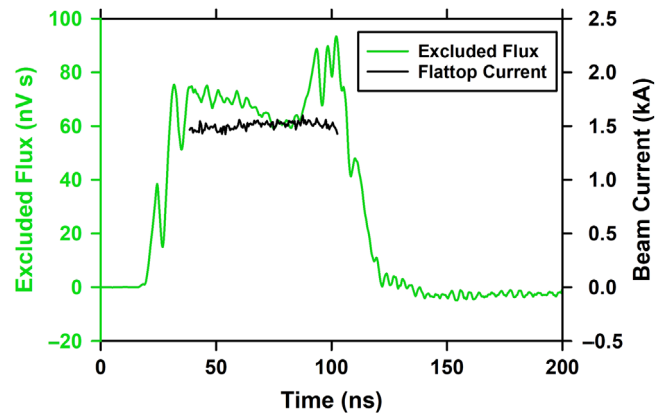


FIG. 7. Excluded flux (green curve) and flattop beam current (black curve). The data for this plot were from shot 37858 corrected for a background shot 37853.

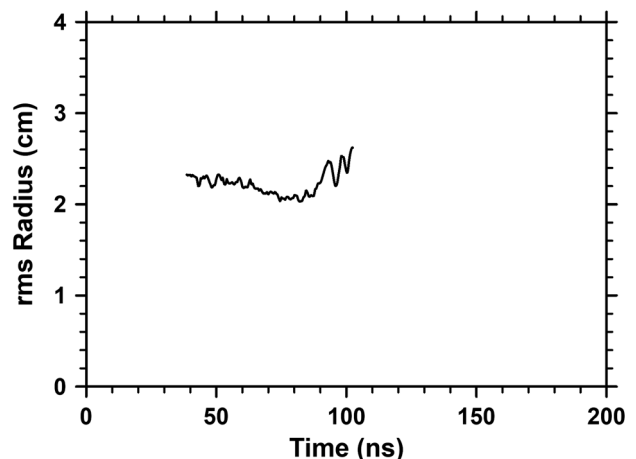


FIG. 8. Beam rms radius measured by the DML for shot 37858.

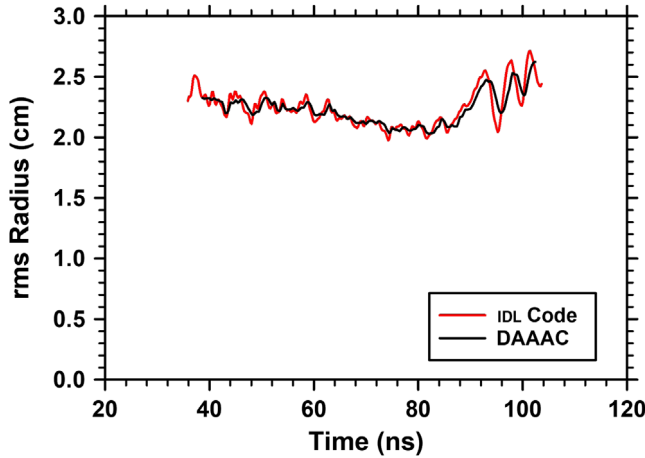


FIG. 9. Comparison between the rms radius calculated by hand using DAAAC (black curve) and our IDL [25] code dml22zeta.pro (red curve) for shot 37858. (Note the expanded time scale).

We developed an IDL [25] code that was used to calculate time-resolved radii for the remainder of the shots. The IDL code follows the same analysis procedure as the hand calculation, using the data from a proximate shot with no DML bias field applied for the background to be subtracted. A comparison between the IDL code and the DAAAC hand calculation for shot 37858 is shown in Fig. 9. The differences in results between the two methods are strictly due to differences in numerical methods between DAAAC and IDL.

D. Uncertainties

The IDL code was used to calculate the time-resolved excluded flux for the remainder of the shots in this initial experimental run. The nonsystematic uncertainty of these measurements can be summarized by the deviation from averages over the flattop current. Table V shows these, as further averaged over shots with the same settings, along with the shot-to-shot percentage standard deviation of averages. Thus, the table includes a measure of reproducibility of beam parameters, which were evidently reproducible to better than $\pm 6\%$ during this experimental run.

The nonsystematic uncertainty of these measurements can be summarized by the deviation from averages over the flattop current. Table VI shows these, as further averaged over shots with the same settings, again with shot-to-shot reproducibility shown as percentage standard deviations.

TABLE V. Average excluded flux (nV s).

		DML bias field, B_0 (G)		
		50	100	200
DT-1 (kG)	0.8	$16.5 \pm 5.1\%$	$35.7 \pm 5.3\%$	$70.0 \pm 2.2\%$
	1.1	13.7	26.1	46.9
	1.4	$9.16 \pm 4.4\%$	$17.7 \pm 2.2\%$	$33.7 \pm 3.0\%$

TABLE VI. Average rms radius (cm).

		DML bias field, B_0 (G)		
		50	100	200
DT-1 (kG)	0.8	$2.16 \pm 2.7\%$	$2.24 \pm 3.1\%$	$2.23 \pm 1.0\%$
	1.1	1.98	1.93	1.83
	1.4	$1.61 \pm 2.6\%$	$1.57 \pm 1.4\%$	$1.54 \pm 1.7\%$

TABLE VII. Average rms variation over flattop (%).

		DML bias field, B_0 (G)		
		50	100	200
DT-1 (kG)	0.8	$10.2 \pm 4.0\%$	$7.13 \pm 11.5\%$	$6.96 \pm 5.0\%$
	1.1	9.80	8.62	9.65
	1.4	$14.7 \pm 12\%$	$13.3 \pm 4.0\%$	$14.4 \pm 4.6\%$

Apparently, the uncertainty in average radii measured by the DML is less than $\pm 4\%$.

The 10%–15% variation of beam radius during the current flattop shown in Fig. 8 can be quantified by the rms deviation from the mean. This is shown in Table VII for each of the magnet settings and the standard deviation from the mean. The highest shot-to-shot variation ($\pm 12\%$) is for the lowest S/N data set ($B_0 = 50$ G, DT-1 = 1.45 kG) as might be expected.

The theoretical basis of interpretation of excluded flux in terms of beam size was validated by these results. For this, the scaling of measured excluded flux or rms radius was established for various DT-1 and DML magnetic fields. Scaling of excluded flux instead of beam size eliminates the uncertainty due to using measured beam current and energy in radius calculations.

E. Excluded-flux scaling: DML bias field

According to Eq. (13), the excluded flux should scale linearly with the bias field. Using excluded flux for this scaling study eliminates the uncertainties associated with the time correlation of the data from the BPMs. This theoretical scaling is corroborated by plotting excluded flux vs bias solenoid setting for each setting of DT-1. Figure 10 shows excluded flux averaged over the current flattop presented in Fig. 7. Also shown are linear least square fits, from which it is clear that the results follow the theoretical linear scaling. Thus, even at the maximum strength, the bias magnetic field was too weak to introduce error by focusing the beam to less than its initial radius, which would have resulted in a nonlinear scaling.

F. Beam size scaling: DT-1 focusing

Finally, we compare measured beam radius with DT-1 focusing to show the uncertainty with all measurements of

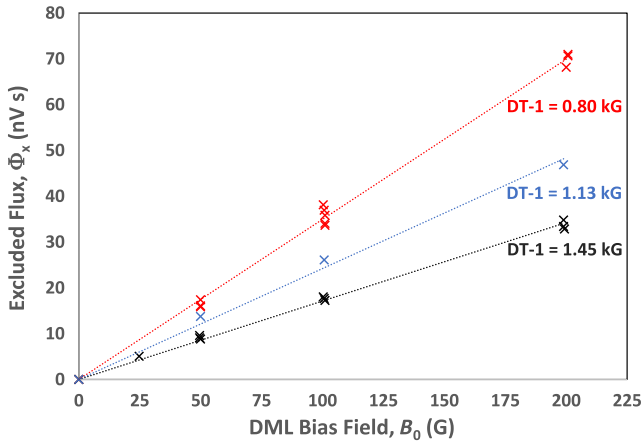


FIG. 10. Average excluded flux as a function of DML bias field for the three peak fields of the DT-1 focusing solenoid. Dotted lines are least-square fits of linear dependence on the bias field.

excluded flux, beam current, and beam energy taken into account. The range of beam sizes for the experiments is illustrated in Fig. 11, which is a plot of the largest and smallest envelope radii calculated by our XTR envelope code [27] for these experimental parameters.

We normally use both envelope and PIC codes to simulate beam transport LIAs [28] and these give slightly different results, so there is an uncertainty in theoretical predictions of beam size at the DML. Moreover, the emittance was not measured during this test, so it is somewhat uncertain. The best fit of the XTR envelope to the DML data would use a normalized 4-rms emittance of 0.71 cm rad. The DT-1 tuning curve simulated by XTR using this emittance is shown in Fig. 12. Considering the number of uncertainties involved, there is reasonable agreement between the DML results and the prediction.

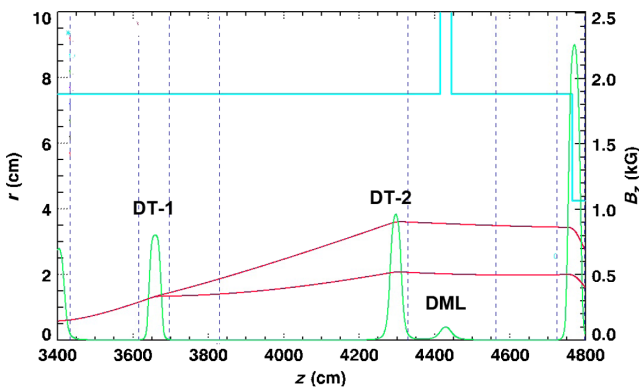


FIG. 11. Beam envelope radius predicted by the XTR code for the maximum DT-1 magnetic field (1.45 kG) and the minimum DT-1 field (0.80 kG) used for these experiments (red curves). Also shown are DST solenoid fields on axis (green curves) and the beam pipe wall (cyan lines). (DT-1 field for maximum beam size is shown). BPM locations are marked with blue dashed lines.

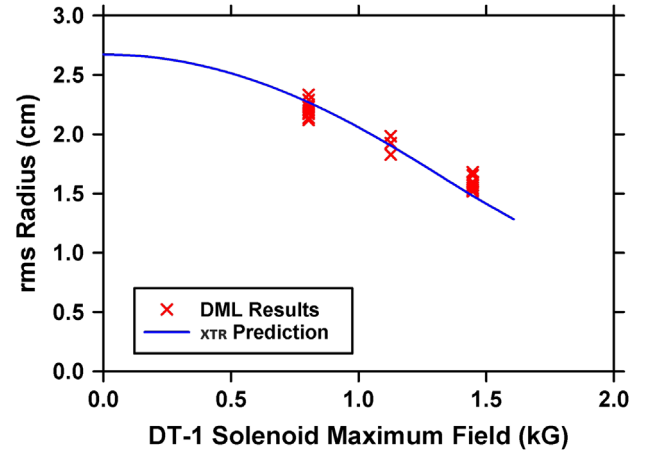


FIG. 12. Tuning curve for DT-1 focusing solenoid showing the beam rms radius predicted by XTR at the DML location for a normalized 4-rms emittance of 0.071 cm rad (blue curve). DML measurements of rms radius averaged over flattop are plotted in red.

Uncertainty of timing of signals leads to large errors during the beam-head rise time and beam-tail fall time, such as calculated displacements and beam size greater than the beam pipe dimensions. Therefore, we have limited our analysis to the flattop region of beam current, which varies by no more than 6% no matter the timing assumed. By doing so, the uncertainty due to timing is less than $\pm 6\%$ for excluded flux and less than $\pm 3\%$ for rms radius. We expect to improve on this in future work, at which time we will revisit the large head-tail excursions.

VII. DISCUSSION

Two results of these experiments deserve further discussion because they have a direct impact on the radiographic spot size and attainable radiographic resolution. These are the time-varying beam radius and the backgrounds observed in the absence of the DML bias field.

A. Time-varying beam radius

In spite of relatively constant beam energy and current during the pulse flattop, these measurements showed a significant variation in beam size. This variation is evident on all of the beams in this experimental run and appears to be fractionally proportional to beam size. For example, Fig. 13 shows the variation in size for all three settings of the DT-1 focusing magnet with $B_0 = 200$ G.

This variation in radius is much larger than the backgrounds we subtracted from the loop flux (Fig. 6). It is also larger than the uncertainty in the measurements. This radius variation contributes directly to the enlargement of the time-integrated radiographic source-spot size, thereby degrading radiographic resolution. Simulations with the XTR envelope code suggest that this temporal variation in beam size would cause a $\pm 6\%$ variation in spot size during

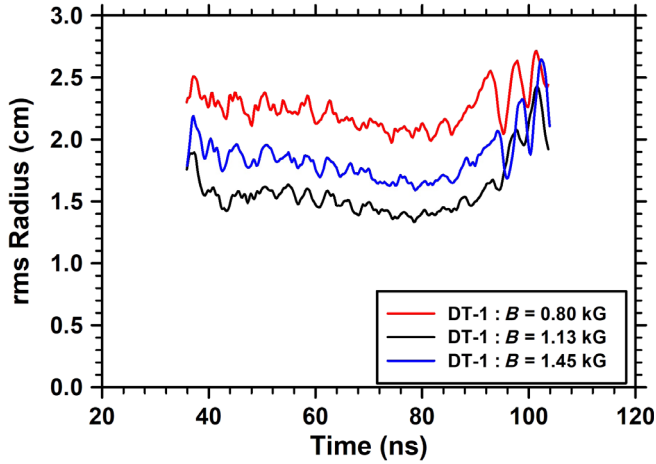


FIG. 13. Beam rms radius for the three settings of the DT-1 focusing solenoid; peak $B = 0.80$ kG (red curve), peak $B = 1.13$ kG (blue curve), and peak $B = 1.45$ kG (black curve).

the flattop alone. Time-resolved measurements of spot size showing the same variation over time support this observation [29]. Including the beam head and tail further enlarges the time-integrated spot size, even though there is less dose rate during those times. Notably, these XTR simulations do not include final-focus solenoid aberrations that would further enlarge the spot size.

The nature of the radius temporal variation is also very reproducible from shot to shot. Figure 14 is a plot of the average of ten of the shots taken with DT-1 set for a peak field of 0.80 kG, also showing the band of uncertainty limited by ± 1 standard deviation. Since beam steering varied considerably during these shots, it appears not to have much effect on the temporal variation. This figure also illustrates the independence of the deduced beam radius on

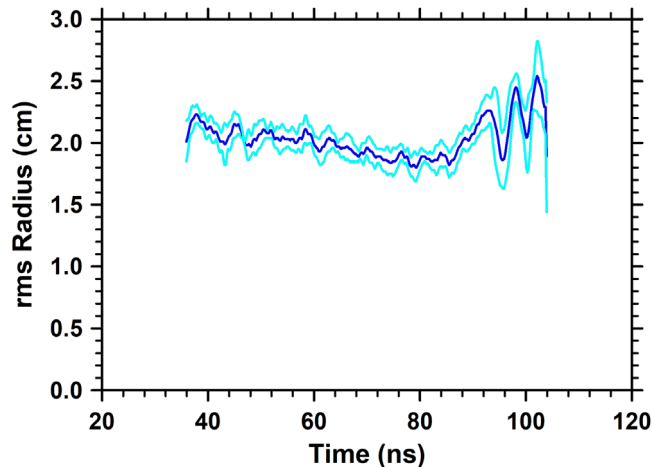


FIG. 14. Average of beam rms radii calculated for ten shots with DT-1 set for a peak field of 0.80 kG (blue curve). These included shots with the DML bias field set to 50, 100, and 200 G. Also shown in cyan is the average ± 1 standard deviation as an indication of the uncertainty of the measurement.

the strength of the DML bias magnetic field, since the ten shots include all three magnetic bias field settings.

Because beam energy during the current flattop is nearly constant, it is unlikely that LIA-transport solenoidal focusing is the cause of such a large variation in beam size. However, the beam dynamics causing the variation of beam size is amenable to simulation with our codes and is under investigation [30]. For example, simulations have shown that time-varying beam neutralization due to ions produced by beam-head spill can be a source of a large variation in size [31,30].

B. Zero-bias background

We corrected our measurements for the persistent low-level background signal observed in data from beam shots with no DML bias magnetic field (Fig. 6). According to Eq. (13), the flux due to rotation of a beam produced by a shielded cathode is proportional to the bias field, so this background was subtracted from measurements with non-zero bias field. This procedure also minimizes contamination by an electrical pickup that is not exactly canceled by our balanced loop flux detection.

Many possible causes of the persistent background were considered and most were rejected based on evidence from data [32]. That the background is related to the beam at the DML location was established by the fact that it was only present when the beam was allowed to exit the accelerator hall (Mode 2). The most likely candidate is imperfect shielding of the cathode. Perfect shielding would require the bucking coil to null the flux linking the cathode, resulting in zero canonical angular momentum, and no rotation of the beam in a field-free drift, hence no diamagnetic flux detected on a background shot.

Violation of the perfectly shielded cathode constraint would add uncertainty to the deduced beam radius. Uncertainty could also result from broken symmetry of the LIA transport, thereby invalidating Busch's theorem. In case either were true, the $<6\%$ background averaged over the current flattop might add as much as 3% uncertainty to the deduced radius. We intend to pursue the possibility for imperfect cathode shielding and transport asymmetry in future experiments.

Another source of beam-generated background is the beam emittance, which is equivalent to the temperature of a non-neutral plasma column. The effective temperature is given by [19]

$$\frac{kT}{m_e c^2} \approx \frac{1}{8\gamma} \left[\frac{\epsilon_n}{R_{\text{rms}}} \right]^2, \quad (17)$$

which is less than 2 eV for our experimental parameters and an insignificant contribution to the background in our experiments.

The final source of beam-generated background that we consider is the so-called “offset-tilt effect.” A straight wire

filament is not a diamagnetic object, yet it can produce a measurable flux through the DML if it is not exactly centered. Likewise, a filamentary beam that is both offset from the axis and tilted in a plane normal to the direction of the offset produces a measurable flux through the DML. Obviously, this flux cannot be included in any calculation of the radius of a nonzero-size beam based on diamagnetism due to beam rotation.

An elementary estimate of the flux produced by a straight current segment can be obtained by considering a short segment of a loosely wound helical coil [21,33]. A more sophisticated approach recognizes it as proportional to the magnetic dipole moment [34]. The elementary magnetic dipole moment for the distribution of charged particles is $\mathbf{m} = I_\theta \mathbf{S}$, where I_θ is the azimuthal component of current around a loop area with a normal vector \mathbf{S} . The moment of the total current distribution is the sum of these incremental moments. The vector potential is $\mathbf{A}(\mathbf{r}) = \mathbf{m} \times \mathbf{r} [\mu_0/4\pi r^3]$, so offset and tilt produces an axially directed moment, which in turn produces an azimuthal component of potential that can be related to the flux, as previously noted. Following through, one finds that the flux scales in proportion to the azimuthal current $\Phi \propto rA_\theta \propto m_z/r \propto rI_\theta$. In Cartesian coordinates, this can be related to the offset and tilt of the current centroid by $\Phi \propto rv_\theta \propto xv_y - yv_x = \beta c[xy' - yx']$.

For our DML, the proportionality constant was established as $\Phi = 0.37[xy' - yx']$ pV s / (A mm mrad) by direct calibration with a straight current-carrying rod [21]. Through the conservation of canonical angular momentum, the offset-tilt flux at the DML is equal to the flux calculated at any nearby BPM. Moreover, the flux is the same for all values of the bias magnetic field, including zero.

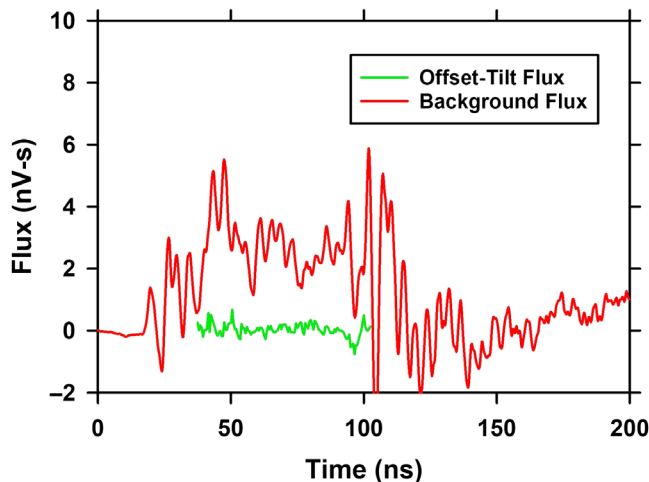


FIG. 15. Flux resulting from offset-tilt effect (green curve) compared with background flux (red curve). The offset-tilt flux is only shown during the current flattop because the calculation is subject to large timing error during the beam rise and fall. (This zero-bias shot 37853 was used as background for shot 37858 analysis).

These conservation arguments facilitate calculating the offset-tilt contribution to the background in our experiments.

Although the beam in our tests was carefully steered to center it at the DML on average, the position varied in time, presumably due to the corkscrew effect [35–37]. However, zero-bias offset-tilt flux due to corkscrew cannot account for the observed persistent background. For example, there are times during the flattop when the beam is centered and the offset-tilt flux vanishes. However, the observed background is never zero. Furthermore, a detailed calculation of the time-resolved offset tilt flux shows it to be less than 10% of the background data used for the DAAAC-analyzed shot 37858 (see Fig. 15) This reinforces our hypothesis that most of the persistent low-level background may be due to imperfect cathode shielding or broken LIA transport symmetry.

VIII. CONCLUSIONS

We have made diamagnetic loop measurements of the size of a relativistic electron beam that agree with beam simulation code predictions. Our measurements correlated well with predicted scaling with bias magnetic field and beam size thereby lending credibility to the technique. The design of this DML apparatus was intended to improve the S/N ratio substantially and it accomplished that goal.

The measured beam size exhibited a large variation during the current flattop, which would affect the radiographic spot size, so should be further investigated.

DML measurements are noninvasive and time resolved. Therefore, they can be used as a real-time monitor to inform an understanding of how time-varying beam size affects radiographic spot size. Moreover, they will improve understanding of beam dynamics producing the varying size.

We corrected our measurements for a persistent background signal observed in data from beam shots with no DML bias magnetic field. Since the flux excluded from the beam by its diamagnetism is proportional to the bias field, this background was subtracted from measurements with a nonzero bias field to obtain the excluded flux. The observed background was too small to account for the apparent time variation of beam size. The beam corkscrew motion of the well-centered beam was shown to account for less than 10% of the observed background through the offset-tilt effect. The remainder can be due to an imperfectly shielded cathode or broken azimuthal symmetry of the external fields and these effects can be explored in future experiments.

Reducing the radius temporal variation and/or the background is expected to reduce the radiographic spot size, thereby improving radiographic resolution.

The DML promises to be a significant aid for tuning an LIA for the highest resolution radiography, and a duplicate of the DML described in this article is planned for installation on the newest radiography LIA now under

development: the four-pulse solid-state powered Scorpius accelerator [38].

ACKNOWLEDGMENTS

The authors thank the entire DARHT-I team for providing the smooth operation of the accelerator necessary for the successful completion of these tests. We are indebted to all those who participated in the design, construction, and calibration of the DML apparatus used for these experiments. This work was supported by the National Nuclear Security Agency of the U.S. Department of Energy under Contract No. 89233218CNA000001.

-
- [1] C. Ekdahl, Modern electron accelerators for radiography, *IEEE Trans. Plasma Sci.* **30**, 254 (2002).
 - [2] K. Peach and C. Ekdahl, Particle beam radiography, *Rev. Accel. Sci. Technol.* **06**, 117 (2013).
 - [3] M. J. Burns, B. E. Carlsten, T. J. T. Kwan *et al.*, DARHT accelerators update and plans for initial operation, in *Proceedings of the 18th Particle Accelerator Conference, New York, 1999* (IEEE, New York, 1999).
 - [4] M. Burns, B. Carlsten, H. Davis, C. Ekdahl *et al.*, Status of the DARHT phase-2 long-pulse accelerator, in *Proceedings of the Particle Accelerator Conference, Chicago, IL, 2001* (IEEE, New York, 2001).
 - [5] C. Ekdahl *et al.*, First beam at DARHT-II, in *Proceedings of the 2003 Particle Accelerator Conference, Portland, OR* (IEEE, New York, 2003).
 - [6] C. Ekdahl *et al.*, Initial electron-beam results from the DARHT-II linear induction accelerator, *IEEE Trans. Plasma Sci.* **33**, 892 (2005).
 - [7] M. Schulze, E. O. Abeyta, P. Aragon *et al.*, Commissioning the DARHT-II scaled accelerator downstream transport, in *Proceedings of the 22nd Particle Accelerator Conference, PAC-2007, Albuquerque, NM* (IEEE, New York, 2007).
 - [8] M. Schulze *et al.*, Commissioning the DARHT-II accelerator downstream transport and target, in *Proceedings of 24th Linear Accelerator Conference (LINAC), Victoria, BC, Canada* (JACoW Publishing, Geneva, Switzerland, 2008).
 - [9] W. E. Quinn, Measurement of plasma beta in high-beta fusion experiments, in *Diagnostics for Fusion Experiments* (Elsevier, Varenna, Italy, 1979), pp. 433–446.
 - [10] C. Ekdahl, M. Greenspan, R. E. Kribel, J. Sethian, and C. B. Wharton, Heating of a Fully Ionized Plasma Column by a Relativistic Electron Beam, *Phys. Rev. Lett.* **33**, 346 (1974).
 - [11] W. E. Nexsen, A non-interfering beam radius diagnostic, Lawrence Livermore National Laboratory Report No. UCRL-JC-108211, 1991.
 - [12] C. Ekdahl *et al.*, Non-invasive measurements of intense relativistic electron beam size, in *Proceedings of the 42nd Annual Meeting of the APS Division of Plasma Physics, Quebec City, Canada, 2000*, <https://flux.aps.org/meetings/YR00/DPP00/abs/S360070.html> [Bull. Am. Phys. Soc. **45**, 105 (2000)]
 - [13] W. E. Nexsen, R. D. Scarpetti, and J. Zentler, Reconstruction of FXR beam conditions, in *Proceedings of the Particle Accelerator Conference, Chicago, IL, 2001* (IEEE, New York, 2001).
 - [14] C. Ekdahl, Non-invasive measurement of electron beam size with diamagnetic loops, *Rev. Sci. Instrum.* **72**, 2909 (2001).
 - [15] W. E. Nexsen, A non-interfering beam radius diagnostic suitable for induction linacs, Lawrence Livermore National Laboratory Report No. UCRL-TR-213331, 2005.
 - [16] F. Mu, Diamagnetic loop diagnoses emittance of intense pulse beam, in *Proceedings of the 17th International Conference on High Power Particle Beams, Xian, China, 2008* (IEEE, New York, 2008).
 - [17] R. B. Miller, *An Introduction to the Physics of Intense Charged Particle Beams* (Plenum Press, New York, NY, 1982).
 - [18] S. Humphries, *Charged Particle Beams* (Wiley, New York, 1990).
 - [19] M. Reiser, *Theory and Design of Charged Particle Beams* (Wiley, New York, NY, 1994).
 - [20] C. A. Ekdahl *et al.*, Non-invasive measurements of intense relativistic electron beam size, Los Alamos National Laboratory Report No. LA-UR-00-4982, 2000.
 - [21] H. V. Smith, W. B. Broste, and C. Ekdahl, A diamagnetic-loop-based beam radius monitor (BRM), Los Alamos National Laboratory Report DARHT Technical Note 507, Report No. LA-UR-21-21491, 2021.
 - [22] S. Humphries, *Field Solutions on Computers* (CRC Press, Boca Raton, FL, 1997).
 - [23] Magnet Design Toolkit, Field Precision, LLC, (2022). [Online]. Available: www.fieldp.com/permag.html.
 - [24] M. J. Burns, H. Davis, C. Ekdahl *et al.*, Overview and status of the dual axis radiographic hydrotest (DARHT) facility, in *Proceedings of 25th International Power Modulator Symposium, Hollywood, CA, 2002* (IEEE, New York, 2002).
 - [25] IDL Software, L3Harris, [Online]. Available: <https://www.l3harrisgeospatial.com/Software-Technology/IDL> [accessed 2022].
 - [26] DAAAC-Data Acquisition Software, Voss Scientific Inc., (2022). [Online]. Available: <https://www.vosssci.com/products/daaac/daaac.html> [accessed 2022].
 - [27] P. Allison, Beam dynamics equations for XTR, Los Alamos National Laboratory Report No. LA-UR-01-6585, 2001.
 - [28] C. Ekdahl, Cathode to target simulations for scorpius: I. Simulation codes and models, Los Alamos National Laboratory Report No. LA-UR-21-21022, 2021.
 - [29] B. T. McCuistian, D. Moir, E. Rose *et al.*, Temporal spot size evolution of the DARHT first axis radiographic source, in *Proceedings of the 11th European Particle Accelerator Conference, Genoa, 2008* (EPS-AG, Genoa, Italy, 2008).
 - [30] M. E. Weller, T. J. Burris-Mog, E. R. Scott, C. A. Ekdahl *et al.*, Beam physics simulations for the Scorpius accelerator, in *Proceedings of 49th International Conference on Plasma Science, Seattle, WA, 2022* (IEEE, New York, 2022).

- [31] C. Ekdahl, Spot-size enlargement due to injector beam spill, Los Alamos National Laboratory Report No. LA-UR-21-21103, 2021.
- [32] C. A. Ekdahl, H. V. Smith, W. B. Broste *et al.*, Diamagnetic loop testing on DARHT-I, Los Alamos National Laboratory Report No. LA-UR-22-24902, 2022.
- [33] T. Tominaka, Vector potential for a single helical current conductor, *Nucl. Instrum. Methods Phys. Res., Sect. A* **523**, 1 (2004).
- [34] L. D. Landau and E. M. Lifshitz, *The Classical Theory of Fields* (Addison-Wesley, Reading, MA, 1962).
- [35] G. Caporaso, W. A. Barletta, D. L. Bix, R. J. Briggs, Y. P. Chong, A. G. Cole, T. J. Fessenden, R. E. Hester, E. J. Lauer, V. K. Neil, A. C. Paul, D. S. Prono, and K. W. Struve, Beam dynamics in the Advanced Test Accelerator (ATA), in *Proceedings of 5th International Conference on High Power Charged Particle Beams, San Francisco, CA, 1983* (IEEE, New York, 1983).
- [36] Y.-J. Chen, Corkscrew modes in linear induction accelerators, *Nucl. Instrum. Methods Phys. Res., Sect. A* **292**, 455 (1990).
- [37] C. Ekdahl, Electron-beam corkscrew motion in an advanced linear induction accelerator, *IEEE Trans. Plasma Sci.* **49**, 3548 (2021).
- [38] M. Crawford, J. Barraza, and C. Ekdahl, Scorpius update: Progress toward a new multi-pulse radiographic system, in *Proceedings of IEEE Pulsed Power Conference, Denver, CO, 2021* (IEEE, New York, 2021).

Correction: Several values given in Table V were incorrect and have been replaced. The value for the proportionality constant given in the first sentence of the seventh paragraph of Sec. VII B was incorrect and has been fixed. The previously published Figs. 10 and 15 also reflected incorrect values and have been replaced.